Modeling the Flash-Heat Experiment on Porous Domains

H.T. Banks[1], D. Cioranescu[2], A.K. Criner[1], and W.P. Winfree[3]

[1] *Center for Research in Scientific Computation*

Department of Mathematics

North Carolina State University

Raleigh, NC 27695-8212

[2] *Laboratoire J. L. Lions*

Université Pierre et Marie Curie

175 rue du Chevaleret

75013 Paris, France

and

[3] *Nondestructive Evaluation Science Branch*

NASA Langley Research Center, MS 231

Hampton, VA 23681

May 2, 2010

Abstract

We discuss several models for a flash-heat experiment in homogeneous isotropic media. We use these to investigate the use of homogenization techniques in approximating models for interrogation via flash-heating in porous materials. We represent porous materials as both randomly perforated domains and periodically perforated domains.

Key Words: Modeling porous media, thermal diffusion, homogenization

1 Introduction

Nondestructive evaluation (NDE) is an important tool in many fields. Nondestructive evaluation is used to identify damage in structures, including components of aircraft, spacecraft, automobiles, trains and piping, as they age beyond their design life. Proper use of nondestructive evaluation can increase the safety and service life of components of many structures. Ultrasound, magnetic particle imaging, eddy current, acoustic emission and radiology are a few examples of NDE techniques. These techniques have been developed in a large number of applications, particularly for homogeneous metallic materials [1]–[5]. Composite materials are increasingly popular in structures including aeronautical and aerospace vehicles and are made with an acceptable level of porosity. This porosity causes a certain amount of noise in the interrogation signal of any NDE technique. In [6] where we investigated using active thermography to detect damage in porous domains we found that we could detect damage of a certain size within a porous medium using thermal interrogation. However, the methods developed in [6] were too computationally intensive to use in the sophisticated parameter estimation routines needed to characterize damage. As in [6] we treat here the problem of modeling the flow of heat in a porous domain but in the current work we focus on the results of homogenization theory (which are less computationally intensive than the methods used in [6]) to capture the behavior.

We aim to use homogenization theory to model a two dimensional cross section version of a flash-heat experiment in porous domains. In Section 2 we discuss the flash-heat experiment in the simple case of isotropic flow in a homogeneous domain and consider several models of the flash-heat experiment. In particular, we present here four different scenarios: (i) heat in a perfectly insulated two dimensional sample (system (2) below); (ii) heat flow in a cross section with part of the boundary held at a fixed temperature (system (4) below); (iii) heat flow in a cross section with loss only in the direction orthogonal to the cross section with boundaries otherwise insulated (system (9) below); and (iv) heat flow in a cross section with small loss on either part or all of its boundary (system (12) and (13), respectively, below). After choosing two

models ((9) and (13)) to investigate in detail, we discuss the procedures used in homogenization to approximate the flow of heat over a domain with random pores by the flow of heat over a domain with many periodically placed pores. One passes this periodic domain to a limit using homogenization theory to gain a limit partial differential equation which replaces the periodically perforated domain with a homogeneous domain that has *anisotropic* flow which approximates the effect of the porosity. With the results of homogenization theory developed in Section 3 we move on to summarize the results of simulations of the flash-heat experiment on a randomly perforated domain, a periodically perforated domain, and a homogeneous domain with the anisotropic flow derived from homogenization theory in Section 4. We also graphically analyze the two example simulations of primary interest in Section 4.

2 Systems

We first recall the system (1) which corresponds to the physical flash-heat experiment described in [6]. This experiment assumes that the temperature of the specimen is within the solid state phase and the boundaries are perfectly insulated. We model the flash-heat experiment on an L_2 (length in the y direction) by L_1 (length in the x direction) rectangle during the time interval $t \in (0, T)$ with $T < \infty$. We refer to the L_1 by L_2 rectangle as $\widehat{\Omega}$ and the four boundaries ω_i, for $i \in \{1, 2, 3, 4\}$. When referring to the entire boundary of $\widehat{\Omega}$, we use $\partial\widehat{\Omega} = \cup_{i=1}^{4}\omega_i$. We take, $L_2 = 1$ mm and $L_1 = 2$ mm. The bottom boundary, $\omega_4 = \{(x, y)|y = 0, x \in (0, L_1)\}$, is heated with heat flux $S_0 = 3.3 \times 10^{-3}\frac{\text{W}}{\text{mm}^2}$ from the initial time, $t_0 = 0$, until t_s and insulated for $t > t_s$. We use an indicator function to describe the flash-heating of the boundary,

$$\mathcal{I}_{[t_0,t_s]}(t) = \begin{cases} 1 & \text{for } t \in [t_0, t_s] \\ 0 & \text{otherwise .} \end{cases}$$

The other boundaries are insulated throughout the experiment. The boundary locations are given in Figure 1. This experiment can be described by the system

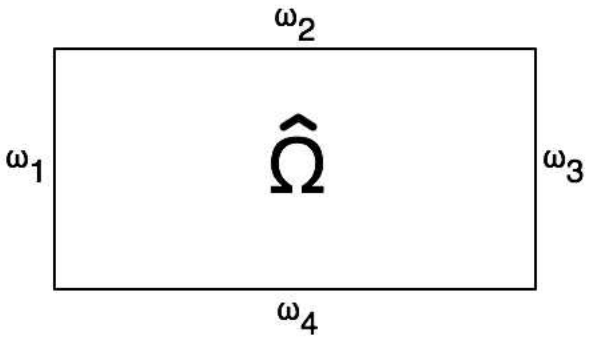

Figure 1: The homogeneous rectangle with boundaries.

$$\begin{cases} c_p \rho \hat{u}_t - k\Delta\hat{u} = 0 & \text{in } \widehat{\Omega} \times (0,T) \\ k\frac{\partial \hat{u}}{\partial \eta} = S_0 \mathcal{I}_{[t_0,t_s]}(t) & \text{on } \omega_4 \times (0,T) \\ k\frac{\partial \hat{u}}{\partial \eta} = 0 & \text{on } \bigcup_{i=1}^{3} \omega_i \times (0,T) \\ \hat{u}(0,\vec{x}) = u_0 & \text{for all } \vec{x} \in \widehat{\Omega}, \end{cases} \tag{1}$$

with thermal conductivity $k = 3.5 \times 10^{-3}$ J/(mm K sec), specific heat $c_p = 0.75$ J/(g K), material density $\rho = 1.6 \times 10^{-3}$ g/(mm^3), and the dependent variable $\hat{u}$ is temperature in degrees Kelvin. The values used throughout this article are summarized in Table 1. We will now make a few changes to the above system. In the partial differential equation, Δu may be written more generally as $\nabla \cdot (A^0 \nabla u)$, where A^0 is the 2 by 2 identity matrix I_2 in the present section and Section 2. We make this change because subsequently we will replace the identity with another positive definite matrix, which will be derived from homogenization theory. Corresponding to this change, we must also change the boundary conditions, so that the boundary conditions still specify the flux when A^0 is not the identity matrix. Specifically, $\frac{\partial u}{\partial \eta} = n \cdot \nabla u$, where n is the exterior unit normal vector, is replaced with $\frac{\partial u}{\partial \eta_{A^0}} = n \cdot A^0 \nabla u$. For convenience and without loss of generality, we will also translate the temperature so that the initial temperature, which we will take to also be the surrounding temperature, is zero. This corresponds to the change $\bar{u} = \hat{u} - u_0$. We wish to use the thermal

diffusivity, $\alpha = \frac{k}{c_p \rho}$, as a characteristic parameter so our final system is

$$\begin{cases} u_t - \alpha \nabla \cdot \left(A^0 \nabla u \right) = 0 & \text{in } \widehat{\Omega} \times (0,T) \\ \alpha \frac{\partial u}{\partial \eta_{A^0}} = S_f \mathcal{I}_{[t_0,t_s]}(t) & \text{on } \omega_4 \times (0,T) \\ \alpha \frac{\partial u}{\partial \eta_{A^0}} = 0 & \text{on } \bigcup_{i=1}^{3} \omega_i \times (0,T) \\ u(\vec{x},0) = 0 & \text{for all } \vec{x} \in \widehat{\Omega}, \end{cases} \tag{2}$$

where $S_f = \frac{S_0}{c_p \rho}$.

The flash-heat experiment is often used to estimate the parameter α. Data is typically collected from the source boundary (ω_4) or the back boundary (the boundary ω_2 opposite the source boundary). In carrying out parameter estimation, one minimizes the least squares distance (or the Frobenius norm) between the data and the model, where the Frobenius norm of the $m \times n$ matrix A with entries a_{ij} is

$$\|A\|_F = \sqrt{\sum_{i=1}^{m} \sum_{j=1}^{n} a_{ij}^2}. \tag{3}$$

We will use the Frobenius norm of values at nodes on ω_2 and ω_4 and time points to evaluate the difference between models when graphical representations are not sufficient.

For completeness we will additionally discuss three modified systems in Sections 2.1–2.3 which are commonly used to model heat but with different physical assumptions than those of (2). In each of Sections 2.1–2.3, we discuss the finite element solution of the system and the physical relevance of the respective system in representing the flash-heat experiment. Throughout the remainder of this document, we will use the parameter values specified in Table 1 unless otherwise stated.

2.1 System 1

The first modified system we propose restricts solutions of (2) to be in $\mathcal{V} = \{v | v \in L^2(0,T; H^1_{\omega_5}(\widehat{\Omega}), \frac{\partial v}{\partial t} \in L^2(0,T; (H^1_{\omega_5}(\widehat{\Omega}))^\dagger)\}$, where $\omega_5 \subset \omega_2$ and $H^1_{\omega_5}(\widehat{\Omega}) =$

Parameter	Value	Units
$[t_0, t_s]$	$[0, 0.6]$	s
T	5	s
S_f	2.75	K mm/s
α	2.9167	mm^2/s
L_1	2	mm
L_2	1	mm
ω_5	$\{(x,y)\|x \in (1.7, 1.8), y = 1\}$	mm
I_2	$\begin{bmatrix} 1 & 0 \\ 0 & 1 \end{bmatrix}$	

Table 1: Parameter values used throughout this document, unless otherwise mentioned. ω_5 is an interval which corresponds to a small portion of the boundary ω_2, and A^0 is a 2-by-2 positive definite matrix arising from homogenization theory.

$\{w \in H^1(\widehat{\Omega})|w(\vec{x}) = 0, \text{ for } \vec{x} \in \omega_5\}$. Here we denote the topological dual of the space X as $X^\dagger$. Frequently one encounters the notation X^* as the topological dual of X, but we reserve the use of * to represent geometries in the development of homogenization results in Section 3. In the remainder of this section we will take $\omega_5 = \{(x,y)|x \in (1.7, 1.8), y = 1\}$. This can be incorporated succinctly in the system

$$\begin{cases} u_t - \alpha\nabla\cdot\left(A^0\nabla u\right) = 0 & \text{in } \widehat{\Omega}\times(0,T) \\ \alpha\frac{\partial u}{\partial \eta_{A^0}} = S_f\mathcal{I}_{[t_0,t_s]}(t) & \text{on } \omega_4\times(0,T) \\ \alpha\frac{\partial u}{\partial \eta_{A^0}} = 0 & \text{on } \cup_{i=1}^3 \omega_i\backslash\omega_5\times(0,T) \\ u = 0 & \text{on } \omega_5\times(0,T) \\ u(\vec{x},0) = 0. & \end{cases} \tag{4}$$

We will use the finite element method to solve (4). The finite element method approximates the infinite dimensional solution of a partial differential equation with a finite dimensional approximation. The domain $(\widehat{\Omega})$ is discretized using the Delaunay triangulation. The finite dimensional solution is

taken from the space of piecewise two dimensional affine functions, where the solution is affine on each mesh element (see [15] for details). Recall the notation $n = (n_x, n_y)$, where n is the unit outward normal and $\dfrac{\partial u}{\partial \eta_{A^0}} = n \cdot \left(A^0 \nabla u\right)$. The boundary conditions can also be written as

$$\begin{aligned}
\left.\frac{\partial u}{\partial \eta_{A^0}}\right|_{\omega_3} &= a_{11}\frac{\partial u}{\partial x} + a_{12}\left.\frac{\partial u}{\partial y}\right|_{\omega_3} = 0 \\
\left.\frac{\partial u}{\partial \eta_{A^0}}\right|_{\omega_1} &= -a_{11}\frac{\partial u}{\partial x} - a_{12}\left.\frac{\partial u}{\partial y}\right|_{\omega_1} = 0 \\
\left.\frac{\partial u}{\partial \eta_{A^0}}\right|_{\omega_2} &= a_{21}\frac{\partial u}{\partial x} + a_{22}\left.\frac{\partial u}{\partial y}\right|_{\omega_2} = 0 \\
\alpha\left.\frac{\partial u}{\partial \eta_{A^0}}\right|_{\omega_4} &= \alpha\left(-a_{21}\frac{\partial u}{\partial x} - a_{22}\frac{\partial u}{\partial y}\right)\Bigg|_{\omega_4} = S_f \mathcal{I}_{[t_0,t_s]}(t).
\end{aligned} \tag{5}$$

Using Green's identities, we obtain the weak form

$$\int_{\widehat{\Omega}} \phi(\vec{x}) u_t \, d\vec{x} - \int_{\omega_4} \phi(x,0) S_f \mathcal{I}_{[t_0,t_s]}(t)\, dx + \alpha \int_{\widehat{\Omega}} \nabla\phi \cdot A^0 \nabla u \, d\vec{x} = 0$$

or

$$\langle u_t, \phi\rangle - \int_{\omega_4} \phi(x,0) S_f \mathcal{I}_{[t_0,t_s]}(t) dx + \alpha \langle \nabla\phi, A^0 \nabla u\rangle = 0,$$

where $\langle \phi, v\rangle = \int_{\widehat{\Omega}} \phi\, v \, d\vec{x}$. Here ϕ is a member of the space of test functions $H^1_{\omega_5}(\widehat{\Omega}) = \{\phi \in H^1(\widehat{\Omega}) | \phi(\vec{x}) = 0, \text{ for } \vec{x} \in \omega_5\}$, or test functions which satisfy the essential boundary conditions. We approximate u with u_N by

$$u_N(t, \vec{x}) = \sum_{i=1}^{N} T_i^{(1)}(t) \phi_i(\vec{x}).$$

Substituting this expression into the weak form with test functions ϕ_i, $i \in \{1, 2, \ldots N\}$ in the space of two dimensional affine functions that are zero on ω_5 (we refer the reader to [15] for more details on these basis elements and the

time dependent coefficients $T_i^{(1)}(t)$), we have

$$\begin{aligned} \left\langle \frac{\partial}{\partial t}\left(\sum_{i=1}^{N}\phi_i T_i^{(1)}\right), \phi_j \right\rangle &- \int_{\omega_4}\phi_j(x,0)S_f\mathcal{I}_{[t_0,t_s]}(t)dx \\ &+ \alpha\left\langle \nabla\phi_j, A^0\nabla\left(\textstyle\sum_{i=1}^{N} T_i^{(1)}\phi_i\right)\right\rangle = 0. \end{aligned} \tag{6}$$

We may factor the time dependent coefficients $T_i^{(1)}(t)$ of the basis elements $\phi_i(\vec{x})$ from the inner product to obtain

$$\begin{aligned} \sum_{i=1}^{N}\frac{d}{dt}T_i^{(1)}\left\langle\phi_i,\phi_j\right\rangle &- S_f\mathcal{I}_{[t_0,t_s]}(t)\int_{\omega_4}\phi_j(x,0)dx \\ &+ \alpha\textstyle\sum_{i=1}^{N} T_i^{(1)}\left\langle\nabla\phi_j, A^0\nabla\phi_i\right\rangle = 0. \end{aligned} \tag{7}$$

Equation (7) must be true for arbitrary $j \in \{1, 2, \ldots, N\}$ and the system may be written as

$$C_1\tfrac{d}{dt}\vec{T_1}(t) + \alpha M_1\vec{T_1}(t) = S_f\mathcal{I}_{[t_0,t_s]}(t)\vec{f_1}, \tag{8}$$

where C_1 is an $N \times N$ positive definite matrix with elements $c_{ij}^{(1)} = \langle\phi_i, \phi_j\rangle$, M_1 is an $N \times N$ positive definite matrix with elements $m_{ij}^{(1)} = \langle\nabla\phi_i, A^0\nabla\phi_j\rangle$, $\vec{f_1}$ is an N-vector with components $f_i^{(1)} = \int_{\omega_4}\phi_i(x,0)dx$ and $\vec{T_1}$ is an N column vector. We informally verified our calculations of these vectors in the case where $A^0 = I_2$ by comparing them to the corresponding values used to calculate the finite element method solution in MatLab's PDE toolbox.

The physical interpretation of this system is that there is a small portion of the back boundary which is fixed at the ambient temperature. This is not a physically feasible situation. In order to fix the temperature of a boundary, experimentalists typically fix the boundary to be 0 ^{o}C by applying ice. We see in Figure 2 below that setting the temperature to the ambient temperature does not give us the behavior observed in the flash-heat experiment, so we suspect forcing the boundary to be a lower temperature (assuming ambient temperature is above freezing) will further exacerbate these problems. The

rapid decrease of the solution of (4) to zero may be intuitively understood by imagining ω_5 being cooled with ice. The ice will melt until the interior reaches the temperature of the ice, and the resulting water (from the melted ice) is related to the loss of energy over time. We could make ω_5 smaller, but the number of mesh points required would increase significantly to do this and the computational costs could become exorbitant. So to use this model we would have to alter the experimental set-up to accommodate setting a small part of the boundary to a fixed temperature. The inefficacy of this system to capture the behavior of the flash-heat experiment is demonstrated in Figure 2 where we compare the solution of (4) to the solution of (2) with $A^0 = I_2$. In Figure 2(a) and (b), we see that the temperature of the midpoint of both the front and back boundaries go to zero in time. It is also important to note that (4) does not capture the shape of temperature on the back boundary ω_2 at $t = 1$ as we see in Figure 2(c). We chose time $t = 1$ for Figure 2 because it demonstrates the lack of smoothness in the solution though it is still relatively close the the solution of the flash-heat experiment as compared to the solution at $t = 5$ (see Figure 2(a)). Because our colleagues at NASA Langley Research Center do not currently have experiments which fix the temperature of the boundary of a specimen, we will not use (4) in the remainder of this work.

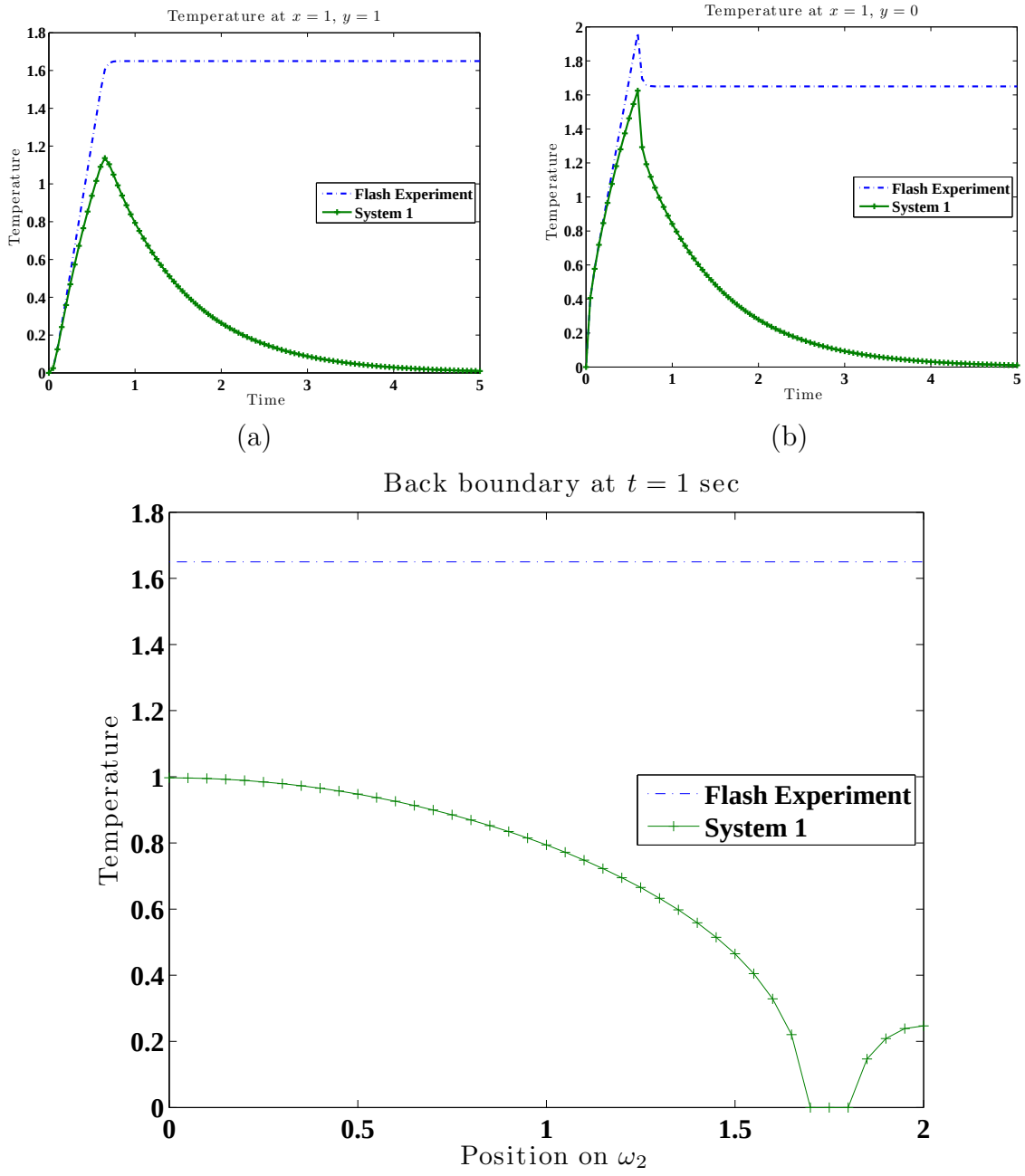

Figure 2: (a) The solutions of (2) and (4) labeled Flash Experiment and System 1, respectively, at the midpoint of the back boundary; (b) The solutions of the (2) and (4) at the midpoint of the source boundary; (c) The solutions of the (2) and (4) on the back boundary at $t = 1$.

2.2 System 2

The second system generalizes the operator $-\nabla \cdot A^0 \nabla$ with the operator $-\nabla \cdot A^0 \nabla + \lambda$ for $\lambda \geq 0$. The difference between the solution of this system and the solution of (2) will depend on the magnitude of λ and clearly there is no difference for $\lambda = 0$. We will use $\lambda = 10^{-2}$ to study the behavior of this system and will further discuss the choice of λ at the conclusion of this section. The modified system

$$\begin{cases} u_t - \alpha \nabla \cdot \left(A^0 \nabla u\right) + \lambda u = 0 & \text{in } \widehat{\Omega} \times (0,T) \\ \alpha \frac{\partial u}{\partial \eta_{A^0}} = S_f \mathcal{I}_{[t_0,t_s]}(t) & \text{on } \omega_4 \times (0,T) \\ \alpha \frac{\partial u}{\partial \eta_{A^0}} = 0 & \text{on } \cup_{i=1}^{3} \omega_i \times (0,T) \\ u(\vec{x},0) = 0, & \end{cases} \tag{9}$$

has a λu term *in* the partial differential equation. The λu term represents loss on the entire specimen in the direction orthogonal to the two dimensional specimen, while there is no loss on the boundary of the specimen.

First, we will consider the numerical solution of (9). Again using the finite element method and the steps detailed in Section 2.1, we begin by finding the weak form of (9) given by

$$\int_{\widehat{\Omega}} \left[\psi \left(u_t + \lambda u\right) + \alpha \nabla \psi \cdot A^0 \nabla u\right] \, d\vec{x} - S_f \mathcal{I}_{[t_0,t_s]} \int_{\omega_4} \psi(x,0) \, dx = 0,$$

with test functions $\psi \in H^1(\widehat{\Omega})$. We chose test functions from $H^1(\widehat{\Omega})$ because there are no essential boundary conditions in this formulation. We replace u with the finite dimensional approximation u_L defined by

$$u_L(x,y,t) = \sum_{i=1}^{L} T_i^{(2)}(t) \psi_i(x,y),$$

where $T_i^{(2)}(t)$ are the time-dependent coefficients of the two dimensional piecewise affine basis elements ψ_i which are described in more detail in [15]. Using

similar calculations as for (4), we have

$$\begin{aligned} \sum_{i=1}^{L}\langle\psi_i,\psi_j\rangle\left(\frac{d}{dt}T_i^{(2)}+\lambda T_i^{(2)}\right) &+ \alpha\sum_{i=1}^{L}\langle\nabla\psi_j,A^0\psi_i\rangle T_i^{(2)} \\ &= S_f\mathcal{I}_{[t_0,t_s]}\int_{\omega_4}\psi_j(x,0)dx, \end{aligned} \tag{10}$$

where $\langle\psi,v\rangle=\int_{\widehat{\Omega}}\psi v\,d\vec{x}$. We write this system as a system of ordinary differential equations

$$C_2\tfrac{d}{dt}\vec{T}_2(t)+\alpha M_2\vec{T}_2(t)=S_f\mathcal{I}_{[t_0,t_s]}(t)\vec{f}_2, \tag{11}$$

where C_2 is an $L\times L$ positive definite matrix with entries $c_{ij}^{(2)}=\langle\psi_i,\psi_j\rangle$, M_2 is an $L\times L$ positive definite matrix with entries $m_{ij}^{(2)}=\frac{\lambda}{\alpha}\langle\psi_i,\psi_j\rangle+\langle\nabla\psi_i,A_0\nabla\psi_j\rangle$, $\vec{f}_2$ is an L-vector with components $f_i^{(2)}=\int_{\omega_4}\psi_i(x,0)dx$ and $\vec{T}_2$ is an L-vector.

As we can see in Figure 3 below, the solution of (9) is more similar to the solution of (2) than is the solution of (4). There will certainly be a decrease in the difference between the solutions of (2) and (9) toward zero as λ goes to zero. Like the solution to (4), solutions of this limit system will approach zero, though it will take much longer than the solution of (4). The decrease of solutions to (9) toward zero is most clear in Figure 3(a) and (b). An advantage of this system is that the shape of the temperature at the boundaries ω_4 and ω_2 is similar in shape to the solution of (2). For instance, in Figure 3(c) where $t=5$ which is the time that gives the largest difference between the two models on the time interval $[0,5]$, the temperature on the back boundary is constant across the back boundary for both the solution of (2) and (9). If we take λ small and the final time T not too large, (9) could be a good approximation of (2). For $\lambda=10^{-5}$, the Frobenius norm of the difference between u^{flash} the solution of (2) and the solution of (9) U at the back boundary ω_2 and source boundary ω_4 are nearly equal and very small. For instance, the Frobenius

norm taken on ω_4 and $t \in [0, 5]$ is

$$\sqrt{\sum_{i=1}^{41}\sum_{j=1}^{101}\left(U(x_i, 0, t_j) - u^{\text{flash}}(x_i, 0, t_j)\right)^2} = 0.0028,$$

where $x_i = \frac{i-1}{20}$ and $t_j = \frac{j-1}{20}$. These advantages in the example where the partial differential equation is defined on a homogeneous rectangle ($\widehat{\Omega}$) with isotropic flow ($A^0 = I_2$) lead us to choose (9) with $\lambda = 10^{-5}$ to model the flash-heat experiment in Sections 3 and 4 where we relax the assumptions on the domain of the partial differential equation and consider anisotropic flow.

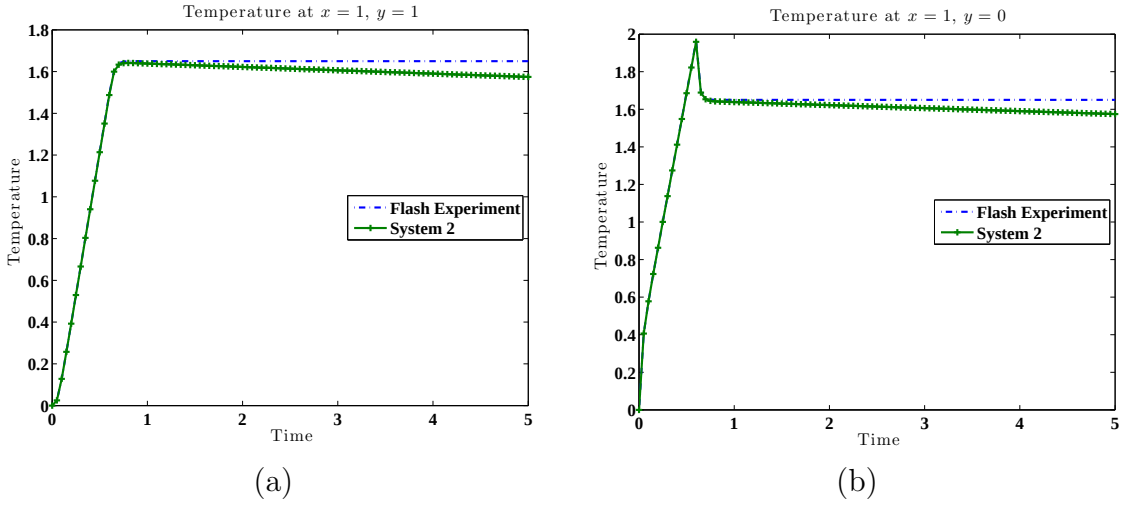

(a) (b)

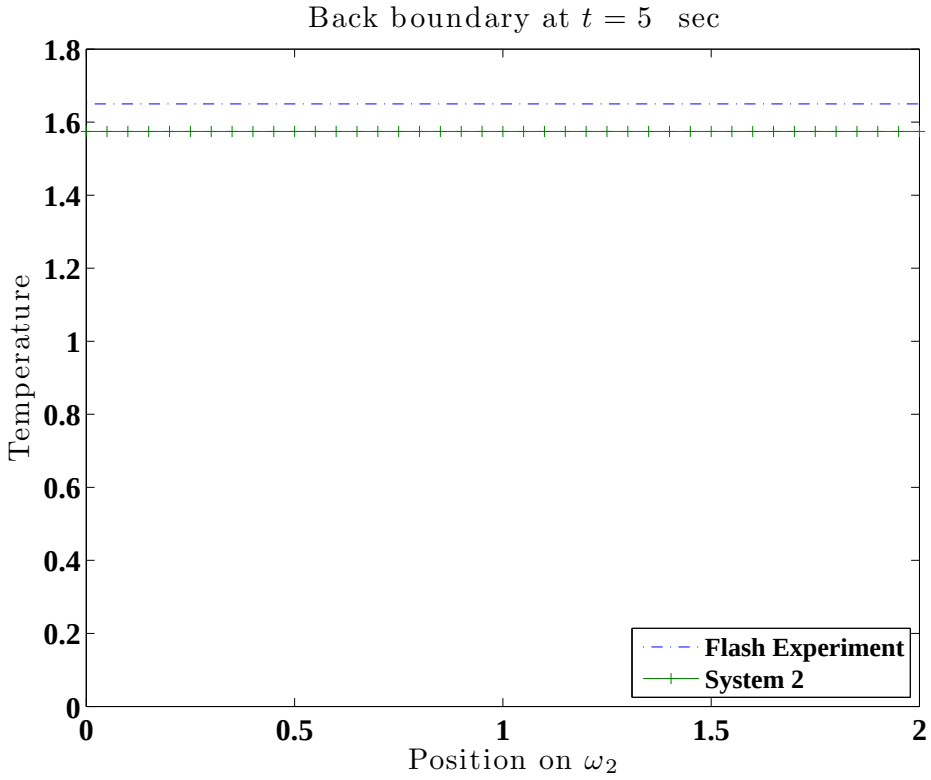

(c)

Figure 3: (a) The solutions of (2) and (9), labeled Flash Experiment and System 2, respectively, with $\lambda = 0.01$ at the midpoint of the back boundary; (b) The solutions of the (2) and (9) with $\lambda = 0.01$ at the midpoint of the source boundary; (c) The solutions of the (2) and (4) with $\lambda = 0.01$ on the back boundary at $t = 5$.

2.3 System 3

The most physically reasonable mathematical model of the flash-heat experiment replaces the zero-flux boundary conditions of (2) with Robin boundary conditions. Robin boundary conditions relax the assumption of perfectly insulated boundaries by assuming Newton cooling occurs on the boundaries. In this section we consider two cases, the first has Robin boundary conditions only on $\omega_5 \subset \omega_2$

$$\begin{cases} u_t - \alpha\nabla\cdot\left(A^0\nabla u\right) = 0 & \text{in } \widehat{\Omega}\times(0,T) \\ \alpha\frac{\partial u}{\partial \eta_{A^0}} = S_f\mathcal{I}_{[t_0,t_s]}(t) & \text{on } \omega_4\times(0,T) \\ \alpha\frac{\partial u}{\partial \eta_{A^0}} = 0 & \text{on } \cup_{i=1}^3 \omega_i\backslash\omega_5\times(0,T) \\ \alpha\frac{\partial u}{\partial \eta_{A^0}} = -\lambda u & \text{on } \omega_5\times(0,T) \\ u(\vec{x},0) = 0, \end{cases} \tag{12}$$

where $\omega_5 = \{(x,y)|x\in(1.7,1.8), y=1\}$. In the second case we include Robin boundary conditions in the entire boundary by incorporating a $-\lambda u$ term in all of the boundary conditions

$$\begin{cases} u_t - \alpha\nabla\cdot\left(A^0\nabla u\right) = 0 & \text{in } \widehat{\Omega}\times(0,T) \\ \alpha\frac{\partial u}{\partial \eta_{A^0}} = S_f\mathcal{I}_{[t_0,t_s]}(t) - \lambda u & \text{on } \omega_4\times(0,T) \\ \alpha\frac{\partial u}{\partial \eta_{A^0}} = -\lambda u & \text{on } \cup_{i=1}^3 \omega_i\times(0,T) \\ u(\vec{x},0) = 0. \end{cases} \tag{13}$$

It is important to recall from earlier in Section 2 that $u = \bar{u} - u_0$ where $\bar{u}$ is the temperature and u_0 is both the initial temperature and the temperature surrounding the specimen. To solve (12) and (13) numerically with the finite element method, we begin with the weak form of (12) and (13)

$$\begin{aligned} \int_{\widehat{\Omega}} \left(\gamma u_t + \alpha\nabla\gamma\cdot A^0\nabla u\right)\, d\vec{x} \quad &- \quad S_f\mathcal{I}_{[t_0,t_s]}(t)\int_{\omega_4}\gamma(x,0)\,dx \\ &+ \quad \lambda\int_{\overline{\partial\Omega}}\gamma u\,ds = 0 \end{aligned} \tag{14}$$

with $\gamma \in H^1(\widehat{\Omega})$, where $\overline{\partial\Omega}$ is ω_5 for (12) and $\partial\widehat{\Omega}$ for (13). We approximate u with u_P defined by

$$u_P(x,y,t) = \sum_{i=1}^{P} T_i^{(3)}(t)\gamma_i(x,y),$$

where γ_i are two dimensional piecewise affine basis elements with time dependent coefficients $T_i^{(3)}(t)$ described in more detail in [15]. After calculations similar to those reported in Section 2.1, we obtain the expression

$$\begin{aligned} &\sum_{i=1}^{P} \frac{d}{dt} T_i^{(3)}(t)\langle\gamma_i,\gamma_j\rangle + \alpha \sum_{i=1}^{P} T_i^{(3)}(t)\langle\nabla\gamma_j, A^0\nabla\gamma_i\rangle \\ &= S_f \mathcal{I}_{[t_0,t_s]}(t) \int_{\omega_4} \gamma_j(x,0)\,dx + \lambda \int_{\overline{\partial\Omega}} \sum_{i=1}^{P} T_i^{(3)}(t)\gamma_j\gamma_i\,ds, \end{aligned} \tag{15}$$

for arbitrary $j \in \{1, 2 \dots P\}$. The resultant system can be written as

$$C_3 \frac{d}{dt}\vec{T}_3(t) + (\alpha M_3 + \lambda D)\,\vec{T}_3(t) = S_f \mathcal{I}_{[t_0,t_s]}(t)\vec{f}_3, \tag{16}$$

where C_3, M_3 and D are $P \times P$ matrices with entries $c_{ij}^{(3)} = \langle\gamma_i,\gamma_j\rangle$, $m_{ij}^{(3)} = \langle\gamma_j, A^0\gamma_i\rangle$, and $d_{ij} = \int_{\overline{\partial\Omega}} \gamma_i\gamma_j\,ds$, respectively, and $\vec{f}_3$ is a P-vector with components $f_j^{(3)} = \int_{\omega_4} \gamma_j(\vec{x})\,ds$.

The boundary conditions in (2) correspond to zero flux on the boundaries, which physically represents perfectly and flawlessly insulated boundaries. The system (12) relaxes the flawless assumption. The Robin boundary conditions imposed on ω_5 in (12) would correspond to a flaw in the insulation at ω_5 which leaches heat with convection heat transfer coefficient λ. The system (13) also relaxes the assumption that the insulation is perfect with the additional λu term in all of the boundary conditions corresponding to an insulating material which has convection heat transfer coefficient λ. The somewhat natural physical interpretation of these two systems is an advantage as compared to the modified systems we considered in Sections 2.1 and 2.2.

In Figure 4 we see that with $\lambda = 0.1$ the solution of (12) over time on the

source and back boundary is quite close the solution of (2). The solution of (13) with $\lambda = 0.1$ and $A^0 = I_2$ decreases toward zero much more than the solution of (13) as is clearly demonstrated at the midpoints of ω_2 and ω_4 in Figures 5(a) and (b), respectively. However, if we decrease λ by a few orders of magnitude, the solution of (13) should possess a decrease similar to the decrease seen in the solution of (12) depicted in Figures 4(a) and (b).

We hope to use the models developed in this effort in the future to model experiments which will be carried out at NASA Langley Research Center. It is a reasonable assumption that the insulating material used in performing the flash-heat experiment will not be damaged–the assumption corresponding to (12), especially as we hope this work may be used to characterize damage in porous materials. However, the assumption that the insulation used in practice is not perfect and allows some exchange of heat between the specimen and the surroundings is not only feasible but inevitable. The Frobenius norm of the difference between u^{flash}, the solution of (2), and U, the solution of (13), on the source boundary ω_4 is sufficiently small for $\lambda = 10^{-5}$. More precisely, $\|U - u^{\text{flash}}\|_F$ on ω_4 and $t \in [0, 5]$ is given by

$$\sqrt{\sum_{i=1}^{41}\sum_{j=1}^{101}\left(U(x_i, 0, t_j) - u^{\text{flash}}(x_i, 0, t_j)\right)^2} = 0.0085,$$

where $x_i = \frac{i-1}{20}$ and $t_j = \frac{j-1}{20}$. The physical relevance of (13) motivates us to use (13) with $\lambda = 10^{-5}$ in addition to (9) with $\lambda = 10^{-5}$ to model the flash-heat experiment in the subsequent sections.

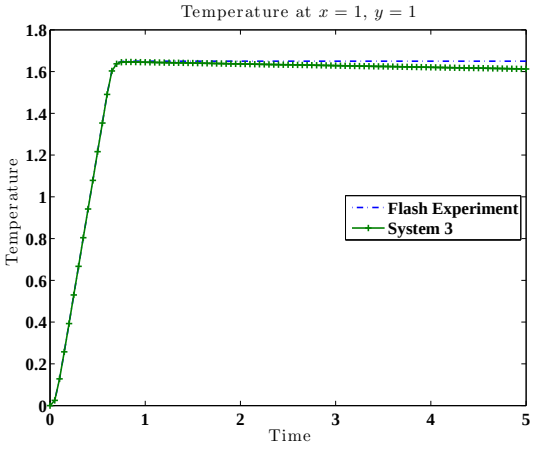

(a)

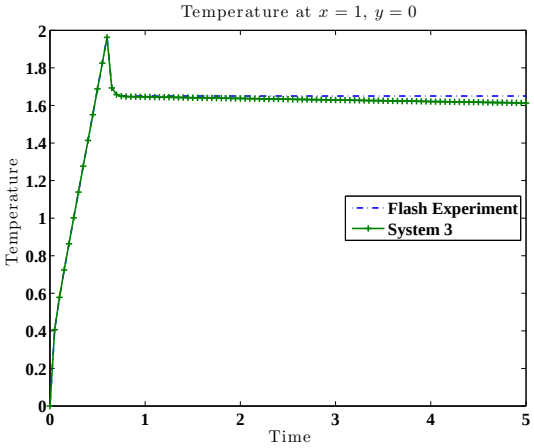

(b)

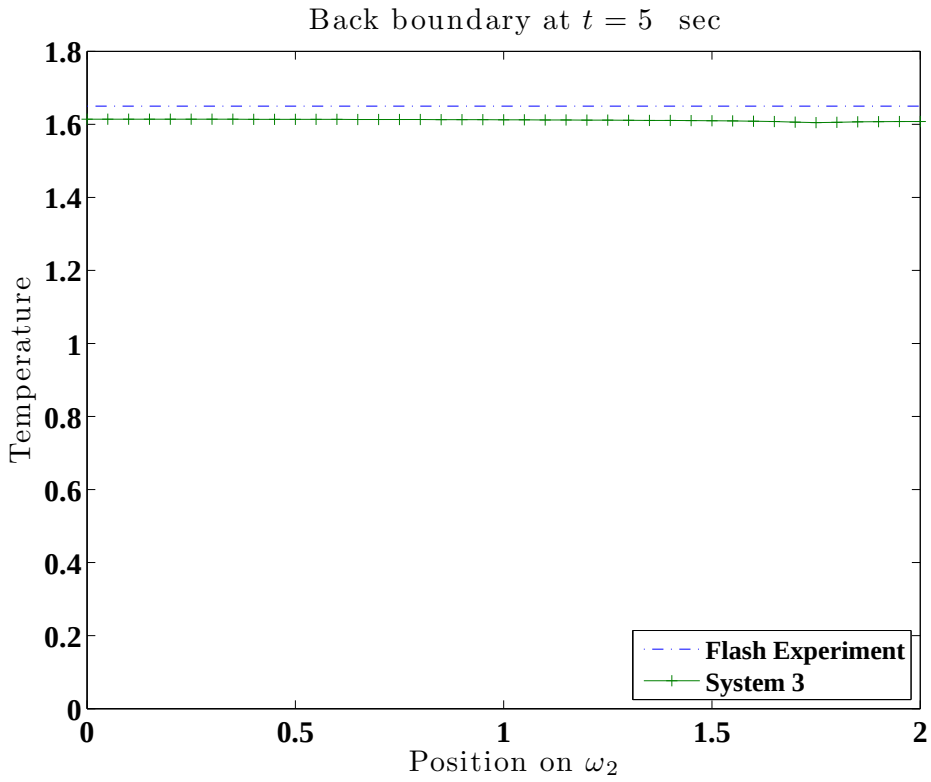

(c)

Figure 4: For $\overline{\partial\Omega} = \omega_5$ and $\lambda = 0.1$ (a) The solutions of (2), labeled Flash Experiment, and (12), labeled System 3, at the midpoint of the back boundary; (b) The solutions of the (2) and (12) at the midpoint of the source boundary; (c) The solutions of the (2) and (12) on the back boundary at $t = 5$.

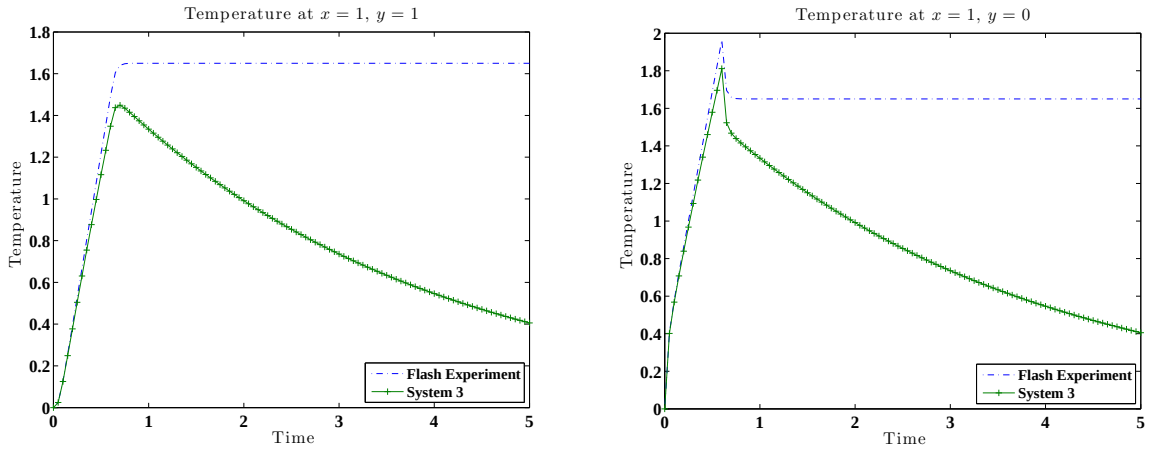

(a) (b)

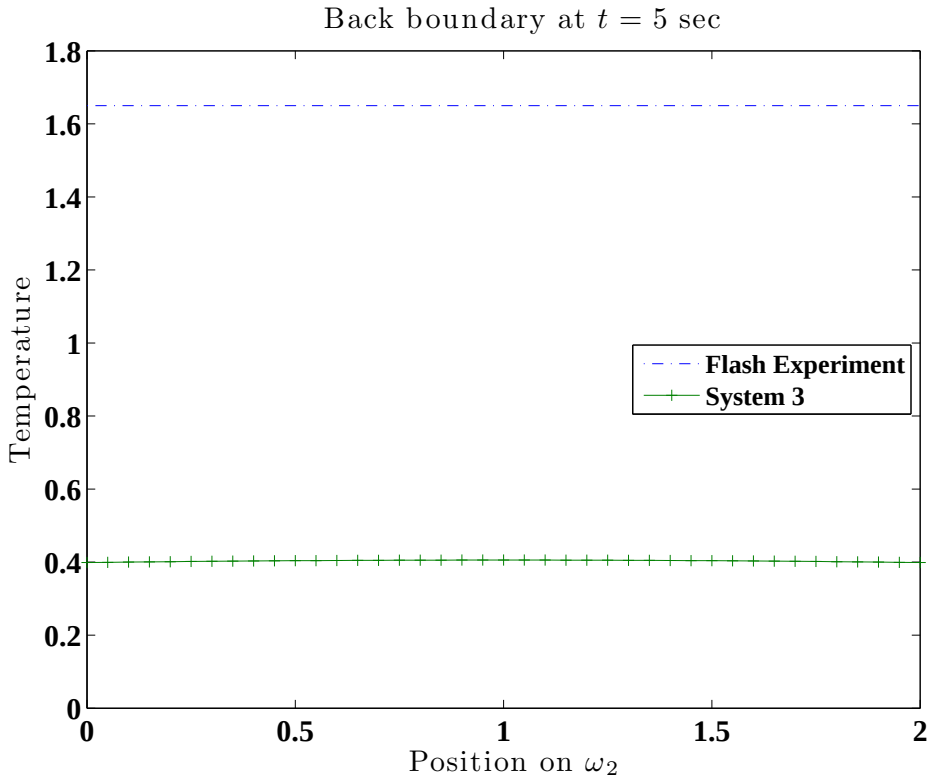

(c)

Figure 5: For $\overline{\partial\Omega} = \partial\widehat{\Omega}$ and $\lambda = 0.1$ (a) The solutions of (2), labeled Flash Experiment, and (13), labeled System 3, at the midpoint of the back boundary; (b) The solutions of the (2) and (13) at the midpoint of the source boundary; (c) The solutions of the (2) and (13) on the back boundary at $t = 5$.

3 Homogenization

Now that we have chosen two systems, (9) with $\lambda = 10^{-5}$ and (13) with $\lambda = 10^{-5}$, which model the flash-heat experiment reasonably well on a homogeneous domain, we will use these two systems to model the flash-heat experiment on more complicated domains than the homogeneous rectangle $\widehat{\Omega}$. We developed a method to model the flash-heat experiment on porous domains in [6]. Though these simulations were useful in detecting damage, they were too computationally intensive for the more sophisticated parameter estimation procedures needed to characterize damage. Here we will use (9) and (13) along with random geometries to model the flash-heat experiment in a porous domain and compare them to limit partial differential equations which are derived from homogenization theory. In this formulation A^0 is no longer I_2 and the random complicated geometry is replaced with a less complicated domain with anisotropic flow. We will focus on values obtained on the source boundary ω_4 when we compare the subsequent models.

We will consider a random geometry Ω (depicted in Figure 6), which is composed of $\widehat{\Omega} \setminus \cup_{i=1}^{n_r} \Omega_i$, where Ω_i are randomly placed pores, $\partial\Omega_i$ is the boundary of the ith pore and ω_i are the same as in the previous sections. For each of the systems (9) and (13) we chose on the homogeneous rectangle $\widehat{\Omega}$, we must now pose the problem on Ω. We will call the dependent variable of this system u^{rand}, where 'rand' refers to the random domain. Here it is worthwhile to note that we have performed the transformations detailed in the beginning of Section 2 to all of the partial differential equations in this section.

The system corresponding to (9) on the random domain Ω is given by

$$\begin{cases} u_t^{\text{rand}} - \alpha\Delta u^{\text{rand}} + \lambda u^{\text{rand}} = 0 & \text{on } \Omega \times (0,T) \\ \alpha \frac{\partial}{\partial \eta} u^{\text{rand}} = 0 & \text{on } \cup_{i=1}^{n_r} \partial\Omega_i \times (0,T) \\ \alpha \frac{\partial}{\partial \eta} u^{\text{rand}} = 0 & \text{on } \cup_{i=1}^{3} \omega_i \times (0,T) \\ \alpha \frac{\partial}{\partial \eta} u^{\text{rand}} = S_f \mathcal{I}_{[0,t_s]}(t) & \text{on } \omega_4 \times (0,T) \\ u^{\text{rand}}(\vec{x},0) = 0, & \end{cases} \tag{17}$$

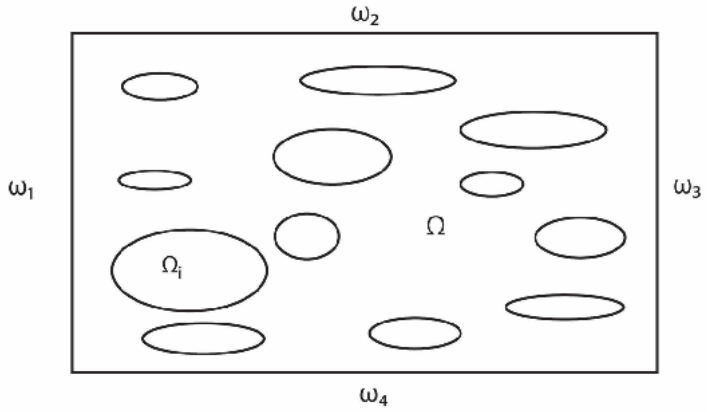

Figure 6: A typical porous domain with random pores (enlarged view)

and the system corresponding to (13) on the random domain Ω is given by

$$\begin{cases} u_t^{\text{rand}} - \alpha \Delta u^{\text{rand}} = 0 & \text{on } \Omega \times (0,T) \\ \alpha \frac{\partial}{\partial \eta} u^{\text{rand}} = 0 & \text{on } \cup_{i=1}^{n_r} \partial\Omega_i \times (0,T) \\ \alpha \frac{\partial}{\partial \eta} u^{\text{rand}} = -\lambda u^{\text{rand}} & \text{on } \cup_{i=1}^{3} \omega_i \times (0,T) \\ \alpha \frac{\partial}{\partial \eta} u^{\text{rand}} = S_f \mathcal{I}_{[0,t_s]}(t) - \lambda u^{\text{rand}} & \text{on } \omega_4 \times (0,T) \\ u^{\text{rand}}(\vec{x},0) = 0. \end{cases} \tag{18}$$

We will use these two systems on random geometries to simulate data that one might expect from the flash-heat experiment performed on porous specimens. We generate these geometries and solve the partial differential equations using the methods developed in [6].

In order to apply homogenization theory to (17) and (18), we will use geometries with enough pores to suppose that Ω has a periodic structure (though it may be that the physical specimens are better modeled with periodic pores as the pores in composite materials are often the result of sinusoidal manufacturing processes). In other words, we suppose that the pores (or holes) are periodically distributed with a period ε, where ε is a small parameter that we let go to zero in the limit. This is the framework of the periodic homogenization theory which is explained in more detail in [11]. To do so, we introduce

a reference cell (or domain) Y. For our purpose, let us take as Y the original (homogeneous) rectangle $\widehat{\Omega}$. Let $B = \cup_{i=1}^{N} B_i$ be a set of N open subsets strictly included in Y such that $B_i \cap B_j = \emptyset$ for $i \neq j$.

Denote by $\tau(\varepsilon\overline{B})$ the set of all translated images of $\varepsilon\overline{B}$ of the form $\varepsilon(\kappa\ell + B)$, $\kappa \in \mathbb{Z}^2$, $\kappa\ell = (\kappa_1\ell_1, \kappa_2\ell_2)$, so the set $\tau(\varepsilon\overline{B})$ represents the periodic pores in $\mathbb{R}^2$. Let B^ε be the set of the holes contained in $\widehat{\Omega}$. With the above choice of Y, and taking for instance $\varepsilon = \frac{1}{\lceil\sqrt{\frac{n_\varepsilon}{N}}\rfloor}$ with $n_\varepsilon \to +\infty$, no hole from B^ε will intersect the boundary $\partial\widehat{\Omega}$. Here $\lceil\cdot\rfloor$ is the nearest integer function. We will set

$$\Omega_\varepsilon = \widehat{\Omega} \setminus \overline{B}^\varepsilon.$$

By this construction, the physical domain Ω_ε is periodically perforated with holes of size of the same order as the period. We are essentially approximating the random geometry Ω with the periodic geometry Ω_ε.

We will use the following notation:

- $Y^* = Y \setminus B$,
- $X^\dagger$, the topological dual space of X
- $\theta = \dfrac{|Y^*|}{|Y|}$, the proportion of the material in the cell Y,
- $|\omega|$ = the Lebesgue measure of any open set ω,
- $\mathcal{M}_\omega(\varphi) = \dfrac{1}{|\omega|}\displaystyle\int_\omega \varphi(x)\,dx$, the mean value of φ on the set ω.

Observe that by construction, θ is also the proportion of the material in Ω_ε for any $\varepsilon > 0$ and the percent porosity $= (1-\theta) \times 100\%$. We are now prepared to consider our two systems on Ω_ε. Using Ω_ε to approximate Ω in (17) we have

$$\begin{cases} u_t^\varepsilon - \alpha\Delta u^\varepsilon + \lambda u^\varepsilon = 0 & \text{in } \Omega_\varepsilon \times (0,T) \\ \alpha\frac{\partial}{\partial\eta}u^\varepsilon = 0 & \text{on } \partial B^\varepsilon \cup_{i=1}^{3} \omega_i \times (0,T) \\ \alpha\frac{\partial}{\partial\eta}u^\varepsilon = S_f\mathcal{I}_{[0,t_s]}(t) & \text{on } \omega_4 \times (0,T) \\ u^\varepsilon(\vec{x},0) = 0, \end{cases} \tag{19}$$

and in (18)

$$\begin{cases} u_t^\varepsilon - \alpha\Delta u^\varepsilon = 0 & \text{in } \Omega_\varepsilon \times (0,T) \\ \alpha\frac{\partial}{\partial\eta}u^\varepsilon = 0 & \text{on } \partial B^\varepsilon \times (0,T) \\ \alpha\frac{\partial}{\partial\eta}u^\varepsilon = -\lambda u^\varepsilon & \text{on } \cup_{i=1}^3 \omega_i \times (0,T) \\ \alpha\frac{\partial}{\partial\eta}u^\varepsilon = S_f\mathcal{I}_{[0,t_s]}(t) - \lambda u^\varepsilon & \text{on } \omega_4 \times (0,T) \\ u^\varepsilon(\vec{x},0) = 0. \end{cases} \tag{20}$$

Both (19) and (20) have unique solutions in the Banach space $\mathcal{W}_\varepsilon = \{v | v \in L^2(0,T;H^1(\Omega_\varepsilon)), \frac{\partial v}{\partial t} \in L^2(0,T;(H^1(\Omega_\varepsilon))^\dagger)\}$. One is then allowed to pass to the limit in (19) and (20) to obtain the limit homogenized systems (for details, we refer the reader to [10, 11, 12]). In particular, these references contain proofs that

$$\widetilde{u}^\varepsilon \rightharpoonup \theta U \quad \text{ weakly in } L^2(0,T;H^1(\widehat{\Omega})), \tag{21}$$

where U is characterized by the unique solution of homogenized problems and $\widetilde{u}^\varepsilon$ is the zero extension of u^ε from Ω_ε to the whole domain $\widehat{\Omega}$.

The limit system corresponding to (19) is given by

$$\begin{cases} \theta U_t - \alpha\nabla\cdot\left(A^0 U\right) + \lambda\theta U = 0 & \text{in } \widehat{\Omega} \times (0,T) \\ \alpha\frac{\partial U}{\partial\eta_{A^0}} = 0 & \text{on } \cup_{i=1}^3 \omega_i \times (0,T) \\ \alpha\frac{\partial U}{\partial\eta_{A^0}} = S_f\mathcal{I}_{[0,t_s]}(t) & \text{on } \omega_4 \times (0,T) \\ U(\vec{x},0) = 0, \end{cases} \tag{22}$$

while the limit system corresponding to (20) is given by

$$\begin{cases} \theta U_t - \alpha\nabla\cdot\left(A^0 U\right) = 0 & \text{in } \widehat{\Omega} \times (0,T) \\ \alpha\frac{\partial U}{\partial\eta_{A^0}} = -\lambda U & \text{on } \cup_{i=1}^3 \omega_i \times (0,T) \\ \alpha\frac{\partial U}{\partial\eta_{A^0}} = S_f\mathcal{I}_{[0,t_s]}(t) - \lambda U & \text{on } \omega_4 \times (0,T) \\ U(\vec{x},0) = 0. \end{cases} \tag{23}$$

In both limit systems the homogenized operator A^0 has constant coefficients and is expressed in terms of the following cell problems defining the "corrector"

functions χ_1 and χ_2:

$$\begin{cases} -\Delta\chi_j = 0 \quad \text{for } j = 1,2 \quad \text{in } Y^* \\ \chi_j \quad \text{is } Y \text{ periodic} \\ \dfrac{\partial}{\partial\eta}(\chi_j - y_j) = 0 \quad \text{on } \partial\Omega_i \\ \mathcal{M}_Y^*(\chi) = 0. \end{cases} \tag{24}$$

Then the homogenized matrix $A^0 = (a_{ij}^0)$ is defined by

$$\begin{aligned} a_{11}^0 &= \theta - \frac{1}{|Y|}\int_{Y^*}\frac{\partial\chi_1}{\partial y_1}dy, \quad a_{12}^0 = -\frac{1}{|Y|}\int_{Y^*}\frac{\partial\chi_2}{\partial y_1}dy, \\ a_{21}^0 &= -\frac{1}{|Y|}\int_{Y^*}\frac{\partial\chi_1}{\partial y_2}dy, \qquad a_{22}^0 = \theta - \frac{1}{|Y|}\int_{Y^*}\frac{\partial\chi_2}{\partial y_2}dy. \end{aligned} \tag{25}$$

It is important to note that $\partial\Omega_i$ in (24) refers to the boundaries of the pores of the *reference cells*, depicted in Figure 7.

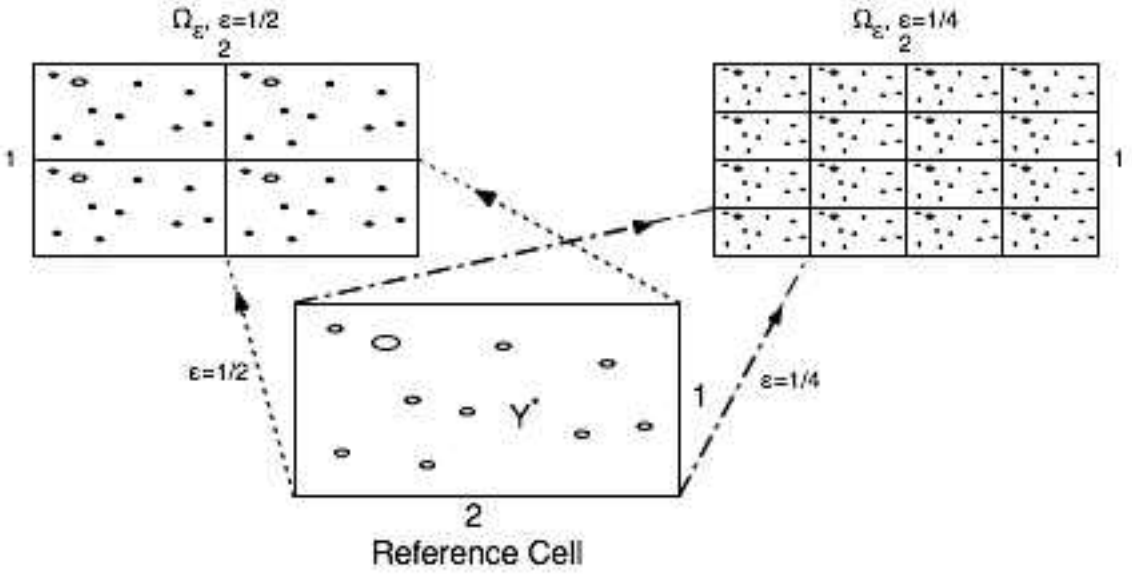

Figure 7: The reference domain and the limit domain with $\varepsilon = \frac{1}{2}$ and $\varepsilon = \frac{1}{4}$.

It can be shown that the error estimate (distance between $\widetilde{u}^\varepsilon$ and θU in the $L^2(0,T;H^1(\widehat{\Omega}))$-norm) is of order of $\sqrt{\varepsilon}$, which completely justifies the homogenization procedure if ε is sufficiently small, or equivalently if the number n_ε of holes is sufficiently large since $n_\varepsilon \sim \dfrac{1}{\varepsilon^2}$. Using the linear trace operator, $\gamma : H^1(\widehat{\Omega}) \to L^2(\omega_4)$ and arguments similar to those in [8], we get the result that $\gamma(\widetilde{u}^\varepsilon)$ converges weakly in $L^2(\omega_4)$ to $\gamma(U)$.

Recalling the convergence of $\widetilde{u}^\varepsilon$ to U, we created numerical simulations to compare U to u^ε and u^{rand} on ω_4. We used methods developed in [6] and [16] to generate the random geometries Ω and Y^*. We used MatLab's PDE toolbox, as in [6], to then solve the partial differential equations on these domains. To calculate U, we used the finite element schemes detailed in Sections 2.2 and 2.3.

For each simulation, letting N be the number of pores in the reference cell, and n_r the number of pores in the random geometry, we might suppose that the ε corresponding to the Ω_ε which approximates Ω is given by

$$\varepsilon = \frac{1}{\lceil \sqrt{\frac{n_r}{N}} \rfloor}, \tag{26}$$

with $\lceil \cdot \rfloor$ representing the nearest integer function. As we see in (26), ε decreases as N decreases. This leads to a subtlety in choosing N. We would like Y^* to capture the random nature of Ω while still containing a sufficiently small number of pores N to ensure ε is small. In the simulations presented here, we take $N = 2$ and use (26) above to calculate u^ε.

4 Results

4.1 Results using systems corresponding to (9)

In the previous section we developed (17) and (with solution u^{rand}) to model the flash-heat experiment in porous material and introcuded (19) (with solution u^ε) to approximate (17). Finally, we introduced homogenization theory to approximate (19) with (22) (with solution U). In this section we will present graphical results corresponding to the three systems and summarize the re-

sults of 200 simulations of the three systems. Here, we will use the parameter values listed in Table 1 with $\lambda = 10^{-5}$. In the next section, we will present similar results but for the more physically relevant system corresponding to the flash-heat experiment on the perforated domain represented by system (18).

We performed simulations of three different porosity levels, 10% (depicted in Figure 8), 5% (depicted in Figure 9), and 2% (depicted in Figure 10). The random geometries used for the examples are featured in Figures 8–10(a), which corresponds to Ω used in (17) to solve for u^{rand}. The approximations of Ω, Ω_ε, are presented for each level of porosity in Figures 8–10(b). Figures 8–10(c) give the solution of u^{rand}, u^ε and U at $y = 0$, $t = 0.1$ on ω_4. We note that U seems to capture the 'average' behavior of u^{rand}, and u^ε. There are several things that we note in Figures 8–10. For instance the solution U to (22) underestimates u^{rand} at the x location where there are pores near ω_4 in the random geometry Ω. For instance, for $\theta = 0.9$ in Figure 8(a) we see large pores near ω_4 at $x = 0.4$ and $x = 1.6$ which correspond to two peaks in u^{rand} where u^{rand} deviates above U at $x = 0.4$ and $x = 1.6$ in Figure 8(c). However, in Figure 8(b) there are no pores in Ω_ε near ω_4 and U appears to overestimate u^ε along the entire interval $x \in [0, 2]$ in Figure 8(c). In Figure 9(a) with $\theta = 0.95$ there are no large pores near ω_4 in Ω and accordingly there are no peaks in u^{rand} away from U though there are a few small bumps of u^{rand} above U at $x = 0.3$ and between $x = 0.75$ and $x = 1$ corresponding to a small pore near ω_4 and a cluster of large pores about 0.05 mm away from ω_4, respectively. Again there are no pores in Ω_ε near ω_4 in Figure 9(b) and u^ε is overestimated by U in Figure 9(c). In Figure 10(b), where $\theta = 0.98$, there are pores very close to ω_4 in Ω_ε and unlike in Figures 8(c) and 9(c) U underestimates u^ε where the pores are close to ω_4 in Ω_ε. In Figure 10(a) there is cluster of pores near ω_4 at $x = 1.6$, which corresponds to a spike in u^{rand} above U in Figure 10(c). It is also worthwhile to note that as θ increases from 0.9 to 0.98, u^{rand} approximates better u^ε which approximates better U in Figures 8–10(c). This suggests that at lower levels of porosity homogenization gives us a better approximation of u^{rand} and u^ε than at higher levels of porosity.

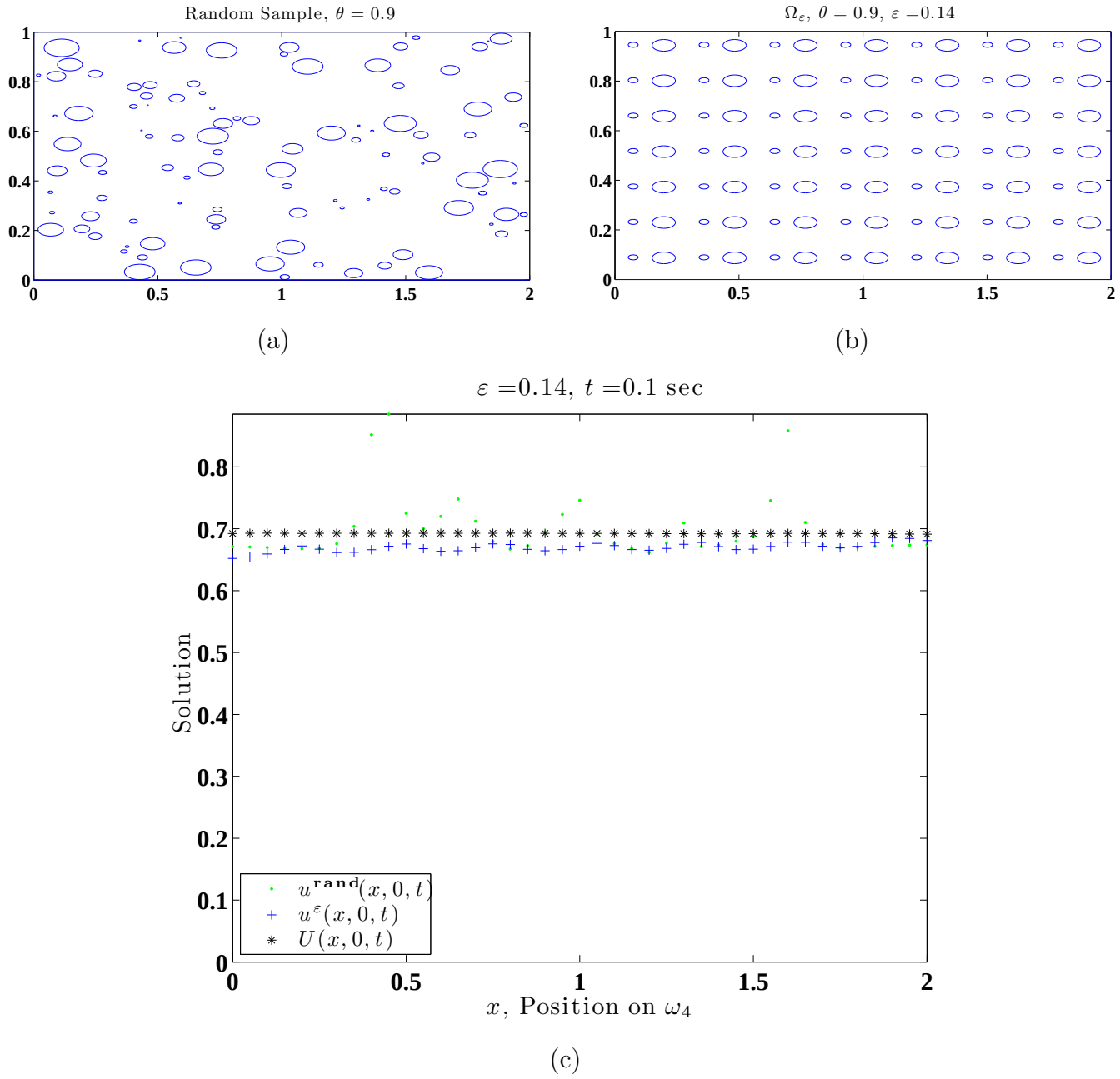

Figure 8: An example simulation at $\theta = 0.9$, or equivalently 10% porosity (a) The random geometry Ω; (b) The geometric approximation of Ω assumed in homogenization theory, Ω_ε where $\varepsilon = 0.14$; (c) $u^{\mathrm{rand}}(x,0,t)$, $u^{\varepsilon}(x,0,t)$, and $U(x,0,t)$ for $t = 0.1$ sec on ω_4. For a better representation of the behavior of the three systems over time on the source boundary (ω_4), see the corresponding movie by **clicking here**.

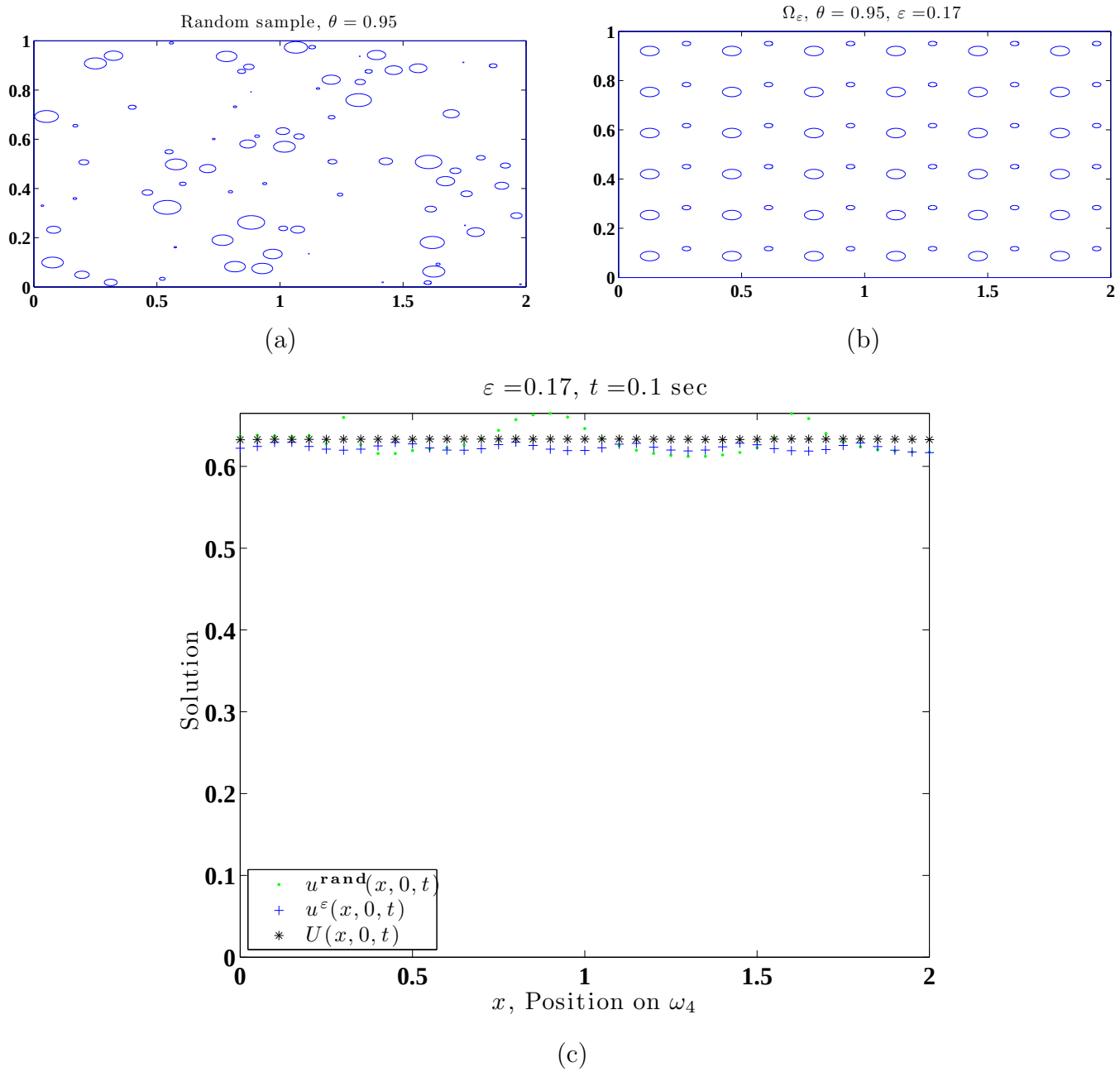

Figure 9: An example simulation at $\theta = 0.95$, or equivalently 5% porosity (a) The random geometry Ω; (b) The geometric approximation of Ω assumed in homogenization theory, Ω_ε where $\varepsilon = 0.17$; (c) $u^{\mathrm{rand}}(x,0,t)$, $u^{\varepsilon}(x,0,t)$, and $U(x,0,t)$ for $t = 0.1$ sec on ω_4. For a better representation of the behavior of the three systems over time on the source boundary (ω_4), see the corresponding movie by **clicking here**..

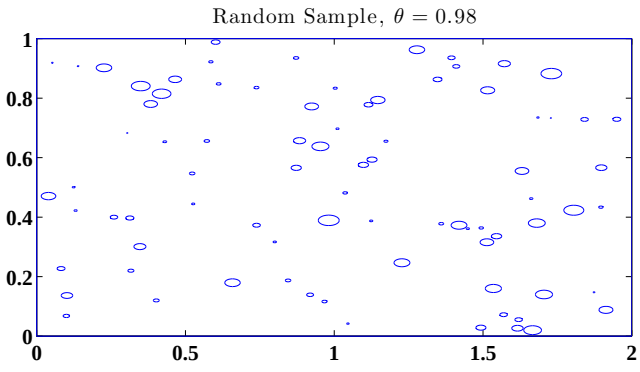

(a)

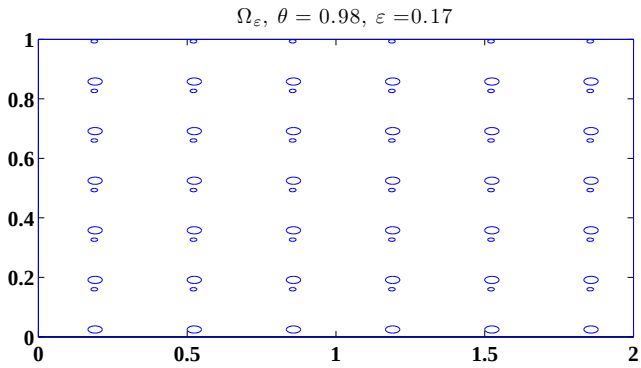

(b)

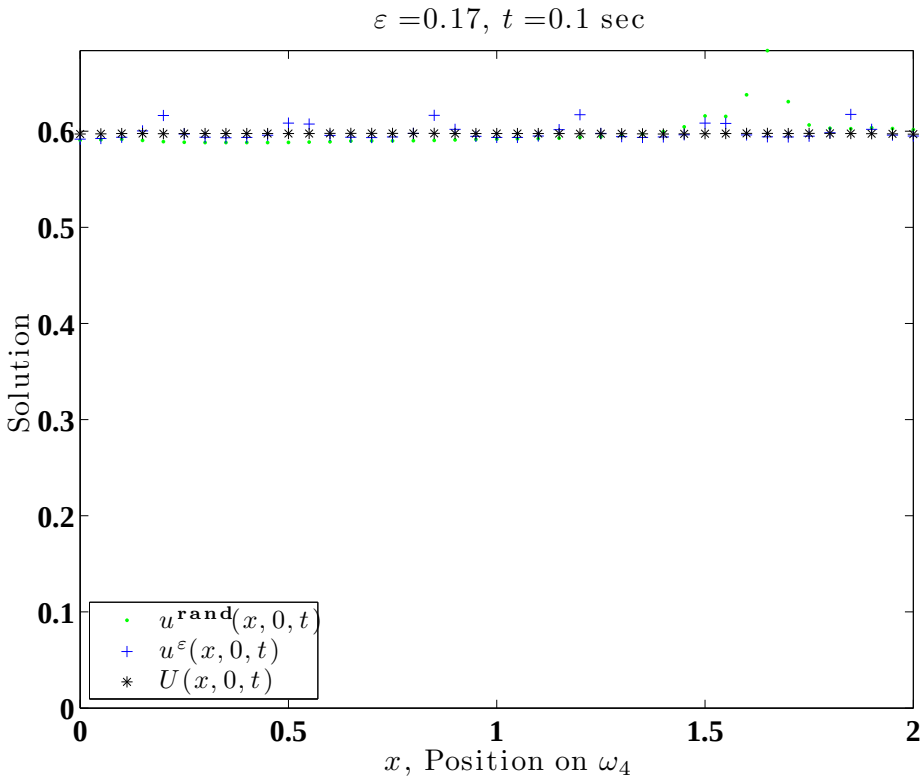

(c)

Figure 10: An example simulation at $\theta = 0.98$, or equivalently 2% porosity (a) The random geometry Ω; (b) The geometric approximation of Ω assumed in homogenization theory, Ω_ε where $\varepsilon = 0.17$; (c) $u^{\text{rand}}(x,0,t)$, $u^{\varepsilon}(x,0,t)$, and $U(x,0,t)$ for $t = 0.1$ sec on ω_4. For a better representation of the behavior of the three systems over time on the source boundary (ω_4), see the corresponding movie by **clicking here**..

	Model	$\theta = 0.9$	$\theta = 0.95$	$\theta = 0.98$
Mean time	u^{rand}	47 sec	51 sec	68 sec
	u^{ε}	23 sec	28 sec	42 sec
	U	4.0 sec	3.8 sec	4.1 sec
Mean mesh size	u^{rand}	7855	8571	10111
	u^{ε}	4882	5780	7484
	U	355	355	355

Table 2: In the first three rows, the last three columns contain the average time for the 200 simulations to calculate the respective solution. The last three rows contain the average mesh size over 200 simulations.

We carried out 200 simulations at each porosity level ($\theta = 0.9, 0.95$ and 0.98) similar to those used to generate Figures 8–10. For each simulation, we selected a random domain Ω and a random reference cell to create the periodically perforated domain Ω_ε. We used these domains to solve for u^{rand}, u^ε and U, as we discussed in Section 3. We recorded the total time to solve each system, the size of the mesh used in the associated finite element method and the Frobenius norm of the difference between solutions on ω_4. In Table 2 we report the average time to solve each of the systems and the average mesh size used to discretize the respective domain. It is clear that of the three systems (17) is the most computationally intensive with a significantly larger mesh than the mesh used to solve for u^ε. The limit system (22) is the least computationally intensive; its mesh is an order of magnitude smaller than the meshes for the other two systems. Also the computing time required to solve (22) for U is five to ten times less than the time to solve (19) for u^ε and ten to fifteen times less time to solve (17) for u^{rand}. This supports the use of the limit system (22) as a more computationally suitable model than (17) and (19).

The limit system (22) seems to be a good approximation of (17) and (19). We evaluate this statement by considering the Frobenius norm. Here the Frobenius norm is taken at time points $t_j = \frac{j-1}{20}$ for $j \in \{1, 2, \dots 101\}$ and nodes $x_i = \frac{i-1}{20}$ for $i \in \{1, 2, \dots 41\}$ along the source boundary ω_4. For each

	$\theta = 0.9$	$\theta = 0.95$	$\theta = 0.98$
Mean $\|u^{\text{rand}} - U\|_F$	1.21	0.630	0.268
St. Dev. $\|u^{\text{rand}} - U\|_F$	0.246	0.106	0.046
Mean $\|u^{\varepsilon} - U\|_F$	1.363	0.669	0.265
St. Dev. $\|u^{\varepsilon} - U\|_F$	0.250	0.128	0.043

Table 3: The first and third row contain the mean Frobenius norm of the difference of the solutions for the 200 simiulations. The second and fourth row contain the standard deviation of the Frobenius norm of the difference of the solutions for the 200 simulations.

simulation, we calculated the Frobenius norm of $\|U - u^{\text{rand}}\|_F$

$$\|U - u^{\text{rand}}\|_F = \sqrt{\sum_{i=1}^{41} \sum_{j=1}^{101} \left(U(x_i, 0, t_j) - u^{\text{rand}}(x_i, 0, t_j)\right)^2}, \tag{27}$$

and $\|U - u^{\varepsilon}\|_F$. We report the average and standard deviation of these quantities for each porosity level in Table 3. As θ increases, U better approximates both u^{rand} and u^{ε}. However, it is not clear whether U better approximates u^{ε} versus u^{rand}.

4.2 Results using systems corresponding to (13)

We next report on computation similar to those in the previous section, but rather than using (17), (19) and (22) as models, we will use (18), (20) and (23). In each figure u^{rand} is the solution of (18), u^{ε} is the solution of (20) and U is the solution of (23). We will consider the three different porosity levels, 10% (or $\theta = 0.9$, depicted in Figure 11), 5% (or $\theta = 0.95$, depicted in Figure 12), and 2% (or $\theta = 0.98$, depicted in Figure 13). The results presented here are for $\lambda = 10^{-5}$ though we carried out calculations for $\lambda = 0$ (the perfectly insulated model) and obtained similar results. The random geometries used for the examples is featured in Figures 11–13(a), which corresponds to Ω used in (18). The approximations of Ω, Ω_{ε}, are presented for each level of porosity in Figures 11–13(b). Figures 11–13(c) give the solutions u^{rand}, u^{ε} and U at $y = 0$, $t = 0.1$ over all values of x on ω_4 or the source boundary. In this case, we see that U seems to capture the 'average' behavior of u^{rand} and that of u^{ε}. We observe similar trends as discussed in the previous section, specifically that U overestimates when there are large pores near ω_4 and underestimates when there are not large pores near ω_4. In Figures 11 with $\theta = 0.9$ we see that the cluster of pores near ω_4 in Figure 11(a) corresponds to U underestimating u^{rand} for x greater than 1.25 in Figure 11(c). There are pores near ω_4 in Figure 11(b) which corresponds to periodic peaks of u^{ε} above U in Figure 11(c). There are pores near ω_4 in Ω_{ε} in Figure 12(b) but they are very small and U overestimates u^{ε} in Figure 12(c). As should be expected for these systems, the difference between the three solutions seems to decrease with porosity. In Figure 13(c) it appears that U is a better estimate for u^{rand} and u^{ε} at $\theta = 0.98$ than it was for $\theta = 0.95$ depicted in Figure 12(c) and $\theta = 0.9$ depicted in Figure 11, so again we see that U is a better approximation at lower levels of porosity or higher values of θ.

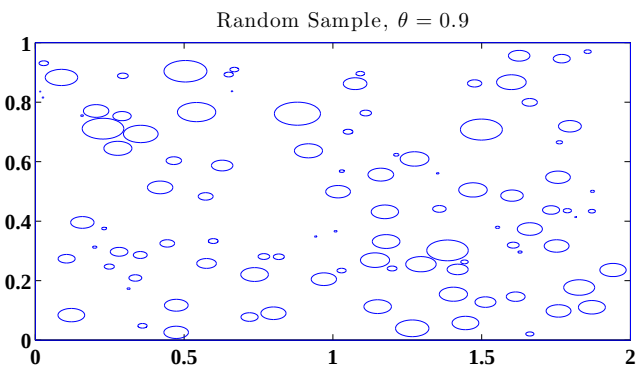

(a)

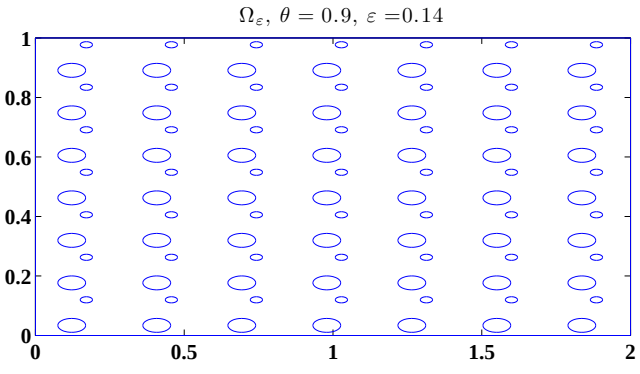

(b)

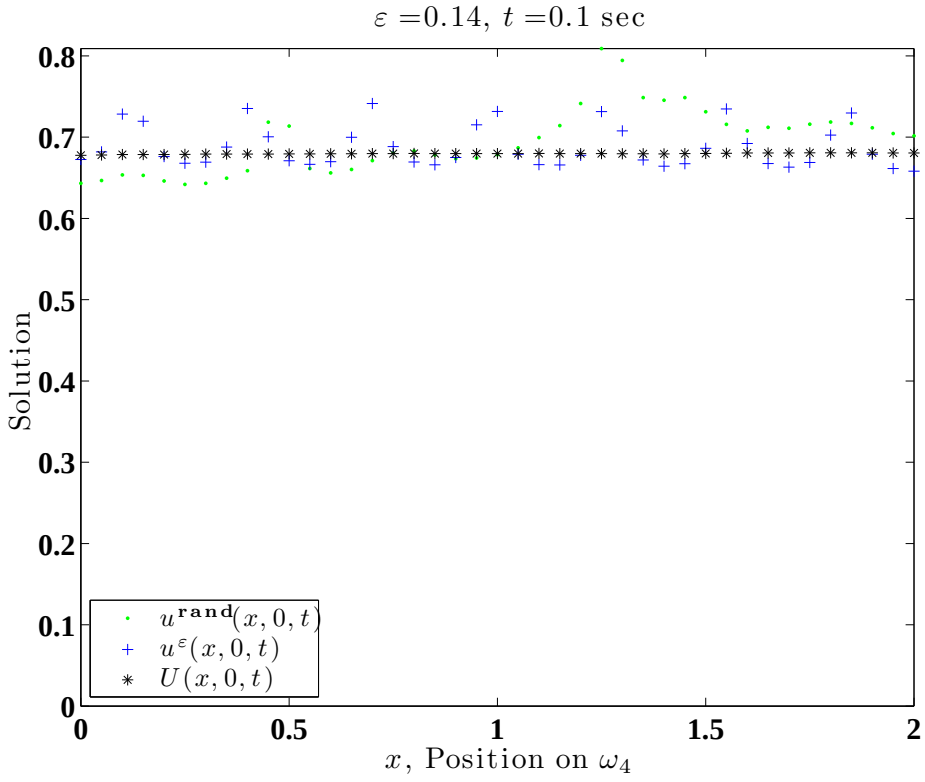

(c)

Figure 11: An example simulation at $\theta = 0.9$, or equivalently 10% porosity (a) The random geometry Ω; (b) The geometric approximation of Ω assumed in homogenization theory, Ω_ε where $\varepsilon = 0.14$; (c) $u^{\mathrm{rand}}(x,0,t)$, $u^{\varepsilon}(x,0,t)$, and $U(x,0,t)$ for $t = 0.1$ sec on ω_4. For a better representation of the behavior of the three systems over time on the source boundary (ω_4), see the corresponding movie by **clicking here**..

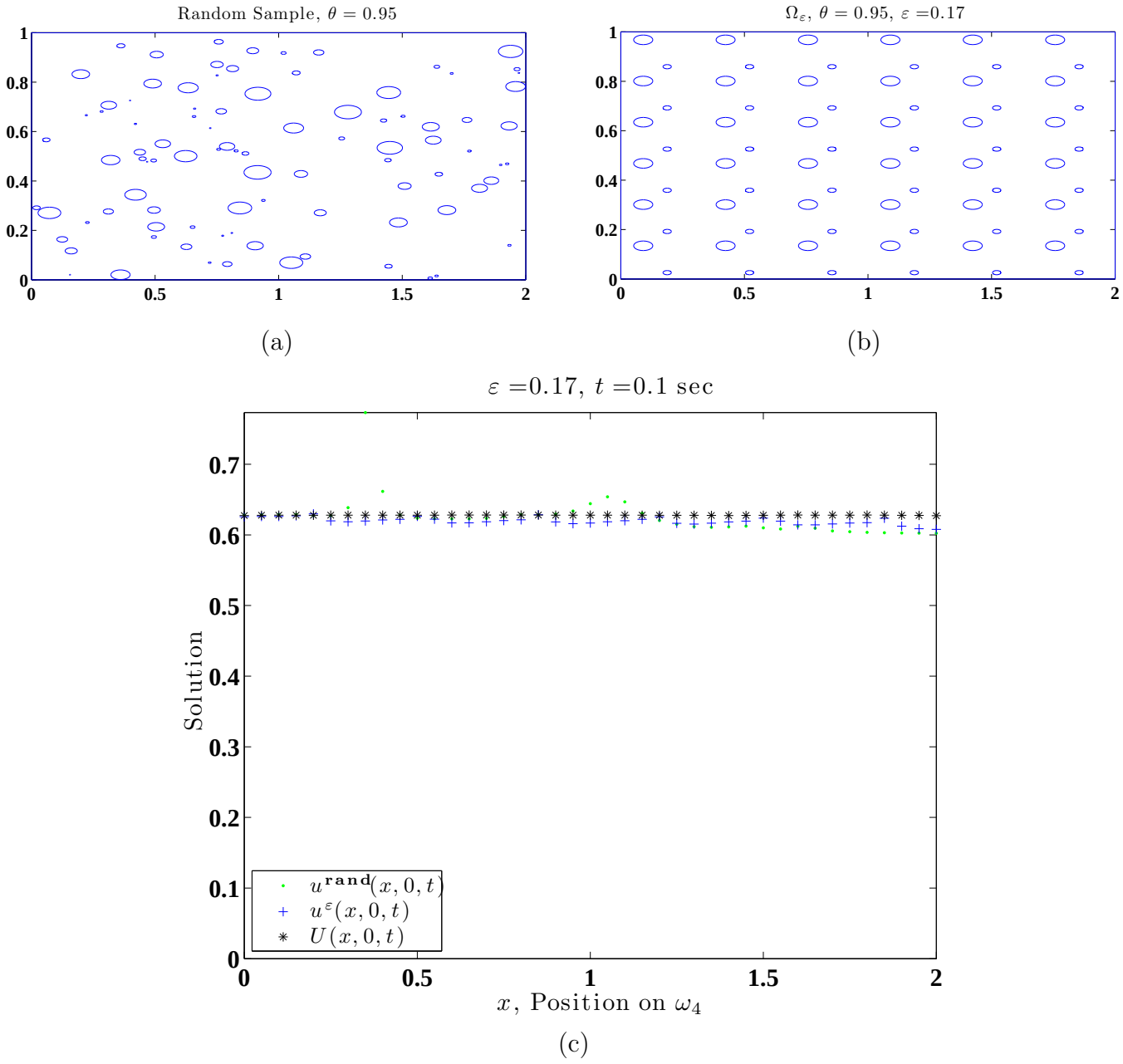

Figure 12: An example simulation at $\theta = 0.95$, or equivalently 5% porosity (a) The random geometry Ω; (b) The geometric approximation of Ω assumed in homogenization theory, Ω_ε where $\varepsilon = 0.17$; (c) $u^{\mathrm{rand}}(x,0,t)$, $u^{\varepsilon}(x,0,t)$, and $U(x,0,t)$ for $t = 0.1$ sec on ω_4. For a better representation of the behavior of the three systems over time on the source boundary (ω_4), see the corresponding movie by **clicking here**.

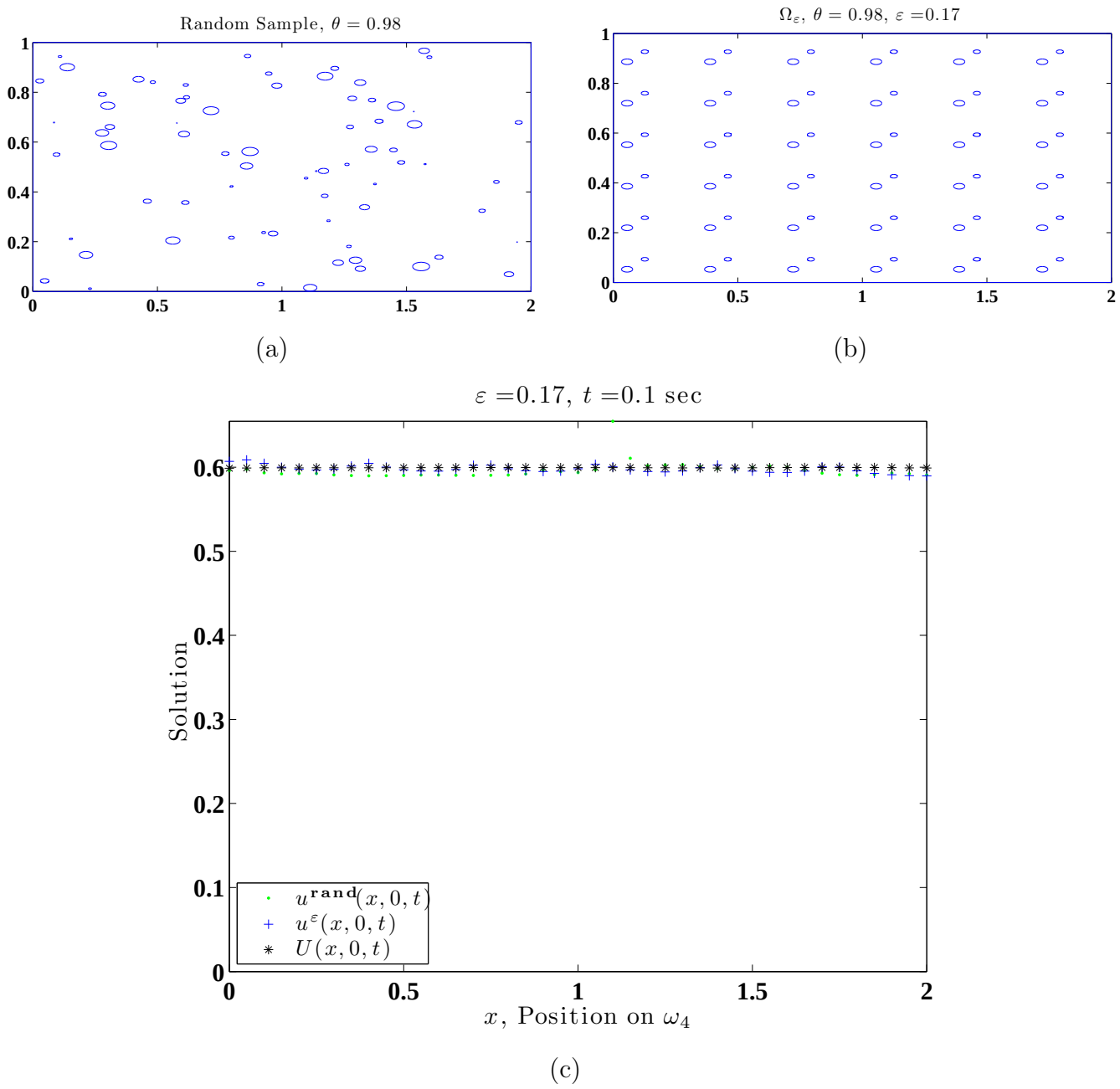

Figure 13: An example simulation at $\theta = 0.98$, or equivalently 2% porosity (a) The random geometry Ω; (b) The geometric approximation of Ω assumed in homogenization theory, Ω_ε where $\varepsilon = 0.17$; (c) $u^{\text{rand}}(x,0,t)$, $u^{\varepsilon}(x,0,t)$, and $U(x,0,t)$ for $t = 0.1$ sec on ω_4. For a better representation of the behavior of the three systems over time on the source boundary (ω_4), see the corresponding movie by **clicking here**.

	Model	$\theta = 0.9$	$\theta = 0.95$	$\theta = 0.98$
Mean time	u^{rand}	45 sec	53 sec	62 sec
	u^{ε}	22 sec	28 sec	37 sec
	U	3.9 sec	4.0 sec	3.7 sec
Mean mesh size	u^{rand}	7851	8551	9965
	u^{ε}	5016	5744	7317
	U	355	355	355

Table 4: In the first three rows, the last three columns contain the average time to calculate the respective solution for the 200 simulations. The last three rows contain the average mesh size over 200 simulations.

We again carried out 200 simulations at each porosity level ($\theta = 0.9, 0.95$ and 0.98) like those used to generate Figures 11–13. For each simulation, we randomly generated the domain Ω on which we solved (18) for u^{rand}. We also created a random Ω_ε, to solve (20) for u^ε. We used the reference cell used to generate Ω_ε to solve (23) for U. In Table 4 we report the average time to solve each of the systems and the average mesh size used to discretize the respective domain. It is clear that of the three systems (18) is the most computationally intensive. The limit system (23) is the least computationally intensive; its mesh is an order of magnitude smaller than the meshes for the other two systems. Also the computing time required to solve for U is five to ten times less than the time to solve for u^ε and ten to fifteen times less time to solve for u^{rand}. This supports the use of the limit system (23) as a more computationally suitable model than (18) and (20).

The limit system (23) seems to be a good approximation of (18) and (20). We consider the Frobenius norm of the difference between the limit systems on the source boundary ω_4. We will take values at time points $t_j = \frac{j-1}{20}$ for $j \in \{1, 2, \ldots 101\}$ and nodes $x_i = \frac{i-1}{20}$ for $i \in \{1, 2, \ldots 41\}$. For each simulation, we calculated the Frobenius norm of $\|U - u^{\text{rand}}\|_F$

$$\|U - u^{\text{rand}}\|_F = \sqrt{\sum_{i=1}^{41} \sum_{j=1}^{101} \left(U(x_i, 0, t_j) - u^{\text{rand}}(x_i, 0, t_j)\right)^2}, \tag{28}$$

and $\|U - u^\varepsilon\|_F$. We report the average and standard deviation of these quan-

	$\theta = 0.9$	$\theta = 0.95$	$\theta = 0.98$
Mean $\|u^{\text{rand}} - U\|_F$	1.21	0.631	0.267
St. Dev. $\|u^{\text{rand}} - U\|_F$	0.245	0.109	0.042
Mean $\|u^{\varepsilon} - U\|_F$	1.322	0.656	0.267
St. Dev. $\|u^{\varepsilon} - U\|_F$	0.258	0.109	0.042

Table 5: The first and third row contain the mean Frobenius norm of the difference of the solutions for the 200 simiulations. The second and fourth row contain the standard deviation of the Frobenius norm of the difference of the solutions for the 200 simulations.

tities for each porosity level in Table 5. As θ increases, U better approximates both u^{rand} and u^{ε}. However, it is not clear that U better approximates either u^{ε} or u^{rand} which is interesting to note but would need a more analytical treatment to investigate.

5 Conclusion and Future Work

We have selected and analyzed two models, which we can use to represent a flash-heat experiment mathematically. The first model, system (9), corresponds to a small loss across the surface of the cross section, and the second, system (13), corresponds to imperfect insulation leading to small loss on all of the boundary of the cross section. We plan to continue to use these in future investigations. In our future efforts though, we will focus on (13) to model the flash-heat experiment as it is a more physically relevant model than (9). The results of homogenization theory in Section 4 are encouraging. It is also clear in Section 4 that the choice of reference domain, specifically the location of pores in Ω_{ε} in relation to the source boundary ω_4 determines the efficacy of U to approximate u^{ε}. Similarly, the location of the pores in Ω in the random domain determine the behavior of u^{rand} in relation to the approximation U. We also observed that U approximates u^{rand} best at the lowest level of porosity, 98% or $\theta = 0.98$. In the future work we would like to use limit system (23) developed in Section 3 as a model to carry out parameter estimation on

data simulated with (18) with added noise to evaluate the use of this work as a model to describe data and eventually characterize damage.

6 Acknowledgments

This research was supported in part by the National Science Foundation under Research Training Grant (RTG) DMS-0636590 and in part by the Air Force Office of Scientific Research under grant number FA9550-09-1-0226.

References

[1] H. T. Banks, N. L. Gibson, and W. P. Winfree, Void detection in complex geometries, Tech. Rep., CRSC-TR08-09, Center for Research in Scientific Computation, North Carolina State University, Raleigh, NC, May, 2008.

[2] H. T. Banks, M. L. Joyner, B. Wincheski, and W. P. Winfree, Nondestructive evaluation using a reduced-order computational methodology, *Inverse Probl.* **16**(4):929–945, 2000.

[3] H.T. Banks and F. Kojima, Boundary shape identification problems in two-dimensional domains related to thermal testing of materials, *Q. Appl. Math.* **47** (2):273–293, 1989.

[4] H. T. Banks and F. Kojima, Identification of material damage in two-dimenstional domains using the SQUID-based nondestructive evaluation system, *Inverse Probl.* **18** (6):1831–1855, 2002.

[5] H. T. Banks, F. Kojima, and W. P. Winfree, Boundary estimation problems arising in thermal tomography, *Inverse Probl.* **6** (6):897–921, 1990.

[6] H.T. Banks, B. Boudreaux, A. K. Criner, K. Foster, C. Uttal, T. Vogel, A.K. Criner, and W.P. Winfree, Thermal based damage detection in porous materials, Tech. Rep., CRSC-TR08-11, Center for Research in Scientific Computation, North Carolina State University, Raleigh, NC, September, 2008; *Inverse Probl. Sci. En.,* to appear.

[7] D. Cioranescu, A. Damlamian, and G. Griso, The periodic unfolding method in homogenization, *SIAM J. Math. Anal.,* **40**(4):1585–1620, 2008.

[8] D. Cioranescu, A. Damlamian, and G. Griso, The periodic unfolding method in domains with holes, to appear.

[9] D. Cioranescu, P. Donato, and R. Zaki, Asymptotic behavior of elliptic problems in perforated domains with nonlinear boundary conditions, *Asymptotic Anal.,* **53**(4):209–235, 2007.

[10] D. Cioranescu and J. Saint Jean Paulin. *Homogenization of Reticulated Structures,* Volume 136 of Applied Mathematical Sciences, Springer–Verlag, New York, 1999.

[11] D. Cioranescu and P. Donato, *An Introduction to Homogenization*, Oxford Lecture Series in Mathematics and Its Applications Volume 27, Oxford University Press, New York, 1999.

[12] P. Donato and A. Nabil, Homogenization and correctors for the heat equation in perforated domains, *Ric. Mat.,* **50**(1):115–144, 2001.

[13] The Mathworks, Inc., *Partial Differential Equation Toolbox 1: User's Guide*, The Mathworks, Inc., Natick, MA, 2008.

[14] W. J. Parker, R. J. Jenkins, C. P. Butler, and G. L. Abbott, Flash method of determining thermal diffusivity, heat capacity, and thermal conductivity, *J. Appl. Phys.* **32** (9):1679–1684, 1961.

[15] Pavel Šolin, *Partial Differential Equations and the Finite Element Method,* John Wiley & Sons, Inc., Hoboken, NJ, 2006.

[16] Wenping Wang, Jiaye Wang, and Myung-Soo Kim, An algebraic condition for the separation of two ellipsoids, *Comput. Aided Geom. D.,* **18**(6):531–539, 2001.